remote sensing

MDPI

Article

On the Validation of the Rotation Procedure from HEE to MEMFA Reference Frame in the Presence of Alfvén Waves in the Interplanetary Medium

Giuseppina Carnevale [1,2] and Mauro Regi [2,*]

[1] Department of Physical and Chemical Sciences, University of L'Aquila, via Vetoio 48, Coppito, 67100 L'Aquila, Italy; giuseppina.carnevale@ingv.it
[2] Istituto Nazionale di Geofisica e Vulcanologia, Viale Crispi 43, 67100 L'Aquila, Italy
* Correspondence: mauro.regi@ingv.it

Abstract: Alfvén waves play an important role in the stability, heating, and transport of magnetized plasmas. They are found to be ubiquitous in solar winds (SW), which mainly propagate outward from the Sun, especially in high-speed streams that originate from coronal holes. When high-speed streams impinge on the Earth's magnetosphere, the impact of Alfvénic fluctuations can cause magnetic reconnections between the intermittent southward Interplanetary Magnetic Field (IMF) and the geomagnetic field, resulting in energy injection from the SW into the Earth's magnetosphere. In this work, we tested a rotation procedure from the Heliocentric Earth Ecliptic (HEE) to the Mean ElectroMagnetic Fields Aligned (MEMFA) reference frame. This is achieved by means of the Empirical Mode Decomposition (EMD) method for both the SW velocity and IMF at 1 AU. Our aim is to check the reliability of the method and its limitations in identifying Alfvénic fluctuations through the spectral analysis of time series in the MEMFA coordinate system. With this procedure, we studied the fluctuations in the main-field-aligned direction and those in the orthogonal plane to the main field. To highlight the peculiarities of each case of study and be able to better identify Alfvén waves when applying this procedure to real data, we reproduced the magnetic and velocity fields of a typical corotating high-speed stream. We tested the procedure in several cases by varying the amplitude of Alfvén waves and noise. We performed the spectral analysis of the Mean Field Aligned (MFA) component of both the magnetic and velocity fields to define the power related to the two main directions: the one aligned to the ambient magnetic field and the one orthogonal to it. The efficiency of the procedure and the results' reliability are supported by Monte Carlo (MC) tests. The method is also applied to a real case that is represented by a selected corotating SW stream that occurred during August 2008, which fell in the solar minimum of solar cycle 23. The results are also compared with those obtained by using Elsässer variables to analyze the Alfvénicity of fluctuations via the normalized cross helicity and the normalized residual energy.

Keywords: MEMFA reference frame; MFA reference frame; EMD method; high-speed streams; solar wind; Alfvén waves; MHD waves simulation; Monte Carlo test

Citation: Carnevale, G.; Regi, M. On the Validation of the Rotation Procedure from HEE to MEMFA Reference Frame in the Presence of Alfvén Waves in the Interplanetary Medium. *Remote Sens.* **2023**, *15*, 4679. https://doi.org/10.3390/rs15194679

Academic Editor: Aleksander A. Ruzmaikin

Received: 7 August 2023
Revised: 30 August 2023
Accepted: 13 September 2023
Published: 24 September 2023

1. Introduction

Solar wind permeates interplanetary space and interacts with the Earth's magnetosphere. Its characteristics change according to the activity of the solar cycle and the structures present in the Sun. The interplay between the coronal magnetic field and SW expansion produces both a highly structured solar corona and a spatially variable solar wind. The interaction between fast solar wind (originating from coronal holes) and slow solar wind (commonly related to closed field line regions) begins in the inner heliosphere; as a consequence of solar rotation, this interaction forms structures that co-rotate with the Sun and have become known as corotating interaction regions (Figure 1). The balance between slow and fast wind changes with solar activity. During solar minima, the occurrence of

corotating streams is more frequent. Such structures propagate and expand throughout interplanetary space, and, at the Earth's orbit (1AU), they are commonly well formed [1,2]. When the fast wind compresses the slow one, it creates a compression downstream, the so-called Corotating Interaction Region (CIR—in red in Figure 1), and a rarefaction region upstream (RR—in pink in Figure 1). The compression region is characterized by an increase in plasma density and magnetic field intensity. Then, this is followed by the High-Speed Stream region (HSS—in blue in Figure 1), which is characterized by high plasma velocity and a reduction in density and magnetic field intensities. The fast wind is typically uncompressive with large Alfvénic fluctuations within it [3]. The RR is characterized by a decrease in plasma velocity and temperature, whereby the density remains low and the fluctuations may be more or less Alfvénic.

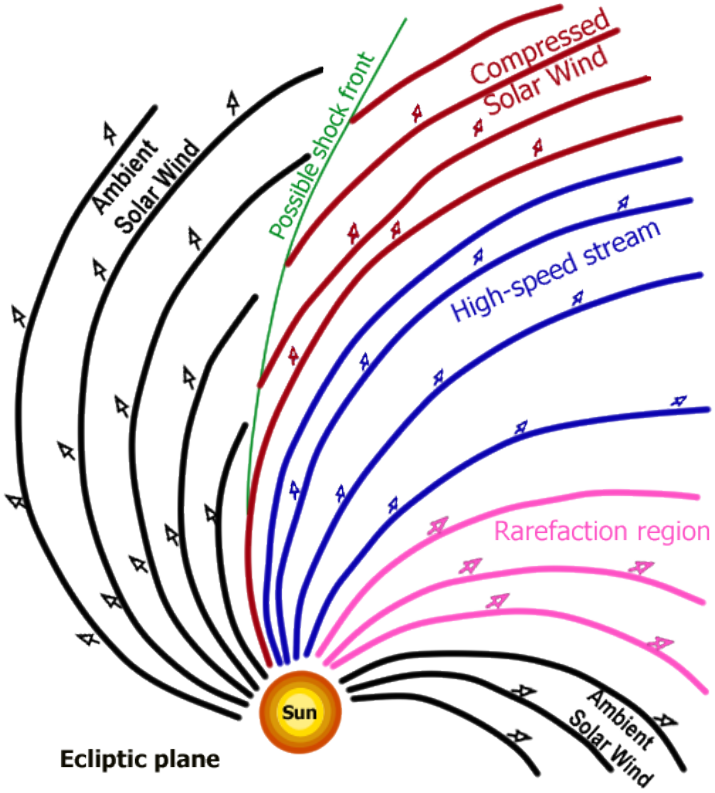

Figure 1. Sketch of a stream structure in the ecliptic plane taken from [4] and adapted from [5]. The spiral structure is a consequence of solar rotation. The spiral inclination changes as the solar wind velocity changes. When the high-speed stream (in blue) compresses the slower ambient solar wind (in black), a compression region downstream (in red) and a rarefaction region upstream (in pink) are formed.

From the first statistical studies conducted by Coleman [6,7], it has been known that fluctuations with periods in the spacecraft frame from 10 to 10^4 seconds are largely due to Alfvén waves [8]. Alfvén waves play an important role in space physics for their contribution to the dynamics and heating of the solar wind. A condition for Alfvén waves in an anisotropic plasma is $\mathbf{v} = \pm(\mathbf{V_A}/\mathbf{B_0})\mathbf{b}$, where $\mathbf{v}$ and $\mathbf{b}$ are the velocity and magnetic perturbations, $\mathbf{B_0}$ is the average magnetic field that is orthogonal to $\mathbf{b}$, and $\mathbf{V_A} = \mathbf{B_0}/(4\pi mn)^{1/2}$ is the Alfvén speed [9] (where m is the proton mass and n is the ion number density $\simeq$ proton number density).

The SW corotating streams and the Alfvén waves within interact with the Earth's environment by energy conversion and transmission through several mechanisms, ranging from particle injection to the MHD waves propagation in the magnetosphere (which are of particular importance at high latitudes). The efficiency in the transfer of energy

generally increases when the southward IMF component (B_z) is negative, leading to the magnetosphere–interplanetary medium coupling. MHD waves are generally classified into frequency bands and distinguished by their morphology. For many decades, particular attention was posed on Ultra Low Frequency (ULF, 1 mHz–5 Hz) waves for their useful contributions in magnetospheric [10–13] and magnetotelluric diagnostics (e.g., [14,15]). It was proved that they are also able to interact with magnetically trapped electrons in the radiation belts leading to particle precipitation toward the high-latitude atmosphere [16–18] with potential effects on the atmospheric dynamics (see [19,20] for a review). In addition, with regard to the Alfvén waves, they can propagate inward to the magnetosphere, when the southward IMF component, with its fluctuations, impinges on the magnetopause during High-Intensity, Long-Duration, Continuous AE Activity (HILDCAA) [21,22]. Alfvén waves, eventually present in the HSS, can contribute to the geomagnetic activity enhancement that is mainly caused by convection processes observed during HILDCAAs [21–24]. As pointed out by [25], it is important to know the interplanetary and SW causes of geomagnetic activity; in particular, in the HILDCAAs case, they are leaded by the southward IMF component of the Alfvén waves within the body of the HSS.

In situ measurements from spacecraft missions provide useful information on such waves, allowing us to understand how they are generated and transmitted to the Earth's magnetosphere. The typical nonlinear character of the wide Alfvénic fluctuations in the SW turbulence [8,26] suggests searching for a suitable method to bring out this kind of wave from the SW signals (in situ measurements). The Empirical Mode Decomposition (EMD) technique allows the analysis of nonlinear and nonstationary signals by decomposing them into components of varying resolutions, and it is therefore suitable for our purposes. In this context, it can be useful to study the MHD waves in a properly defined reference frame, which helps us to distinguish MHD wave properties mainly attributable to compressional or Alfvèn waves.

In particular, in the magnetosphere, where the main magnetic field is larger than its fluctuations, the Mean Field Aligned (MFA) reference frame is generally utilized (e.g., [27–30]). This system is mainly defined by identifying the ambient magnetic field, by separating long periodicity variations from small-time perturbations, using a filtering procedure. Conversely, the Minimum Variance Analysis (MVA, e.g., [31]) and the deHoffman-Teller (HT, [32]) reference frames were also used for studying the interplanetary medium. In the MVA reference frame, the three distinct orthogonal directions are identified by investigating the variances of the magnetic field components. Experimentally, it was demonstrated that it does not necessarily coincide with that of the ambient magnetic field [33,34]. In the HT reference frame, the main direction is the one along which the convection electric field is minimum. The convection electric field in the interplanetary medium represents the Interplanetary Electric Field (IEF)

$$\mathbf{E} = -\mathbf{V} \times \mathbf{B} \tag{1}$$

where **B** and **V** represent the IMF and solar-wind velocity vectors, respectively. Traditionally, both these reference frames are used for studying the properties of MHD wave and non-linear shock waves or discontinuities.

In this work, we want to identify a reference system that is not only able to identify the direction of the main magnetic field but also allows us to choose the second direction of physical relevance. It can be represented by the direction of the main IEF, which is the most geoeffective direction in the vicinity of the Earth's magnetosphere ([35] and reference therein). Based on these aspects, it is clear that the MFA reference frame could be more useful in distinguishing wave properties in the solar wind. However, as mentioned above, the solar wind transfers its energy more efficiently when the B_z component of the IMF is negative, which corresponds to a positive dawn-dusk IEF component. In this work, we proposed a new reference frame based on both the mean directions of IEF and IMF; this new reference frame is hereafter named the Mean ElectroMagnetic Fields Aligned (MEMFA) reference frame.

The efficiency of the MEMFA procedure in separating Alfvén waves from IMF and velocity fluctuations has been verified by means Monte Carlo (MC) test, by simulating synthetic signals in a realistic SW corotating stream. The simulated Alfvén waves also allowed us to compute the power of Alfvénic and compressional fluctuations. The method here proposed seems to be complementary to the traditional one represented by the adiabatic invariant computed from Elsässer variables via the normalized cross helicity and the normalized residual energy [36,37]. The former is related to the degree of correlation between the SW velocity and the magnetic field fluctuations, while the latter is related to the balance between magnetic and kinetic energies. This makes the MEMFA procedure useful for further distinguishing the Alfvénicity in the SW, i.e., the above mentioned peculiar features of SW fluctuations at scales from a few minutes to a few hours [8,34].

In Section 2, we describe the general rotation procedure (Section 2.1), its application to a signal with localized Alfvén waves in the presence of white noise (Section 2.1.1) and red noise (Section 2.1.2). In Section 2.2, we show the MC test and reliability for the procedure in both previous cases. In Section 3, we show the study of both a simulated event (Section 3.1) and a real case event (Section 3.2) and we discuss the comparison of our method with the adiabatic invariants commonly used to describe Alfvénic turbulence. Then, we discuss the results and conclusions in Section 4.

2. Data and Methods

Pure Alfvén waves propagate along the main field direction, with magnetic and velocity perturbations in the plane orthogonal to it. Therefore, a rotation procedure that enables us to identify the main magnetic field direction is a useful tool to identify pure Alfvén waves too. We focused the application on a typical corotating stream because in its high-speed plateau it is well known that there are Alfvén waves ([4,8,26] and references therein); nonetheless, the rotation procedure is very general and can be applied to a general context.

The simulated profiles of SW velocity and IMF time series in Sections 2.1, 2.2 and 3.1 are created accordingly to a typical SW corotating stream. The analysis in Section 3.2 was performed using 1 min averages of magnetic field and plasma measurements during the minimum of solar activity and provided by OMNIWeb (https://cdaweb.gsfc.nasa.gov/, accessed on 21 October 2023), time-shifted to the Earth's bow shock nose. Initial data are given in the HEE coordinate system that has its $\hat{x}$ axis towards the Earth, its $\hat{z}$ axis perpendicular to the ecliptic plane (positive North) and the $\hat{y}$ axis to complete the orthogonal right-handed frame. This system is schematically represented in Figure 2. The HEE system is fixed with respect to the Sun–Earth line. On the other hand, the use of a Lagrangian coordinate system, which is constructed with the axis related to the main physical quantities we deal with, can be very useful to study the physical phenomena that occur. The MFA (Main Field Aligned) coordinate system, widely utilized in the magnetosphere [27,33], can be well applied in the solar wind because the procedure is able to reconstruct the main field by specifying the time scales of interest. In this work, we define a new specific MFA reference frame, the MEMFA (Mean ElectroMagnetic Fields Aligned) in Section 2.1.

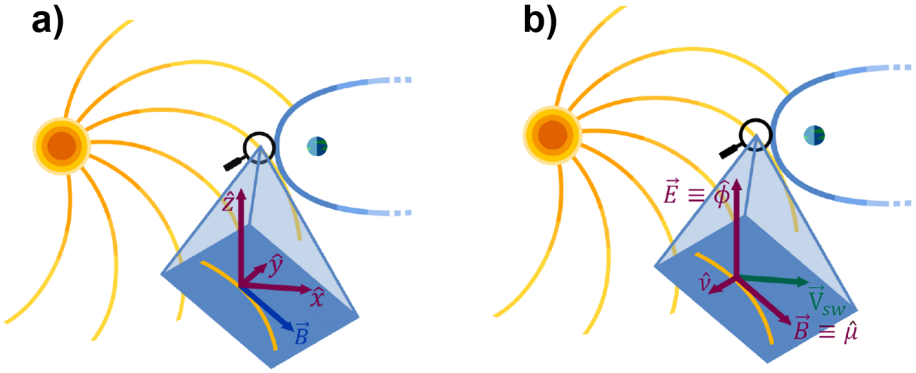

Figure 2. Both pictures represent the ecliptic plane in the background, with the Sun on the left and the Earth with its magnetosphere on the right, and a 3D magnification in the foreground. Panel (**a**): the HEE reference frame . The $\hat{\mathbf{x}}$ axis goes from the Sun toward the Earth, the $\hat{\mathbf{z}}$ axis is perpendicular to the ecliptic plane (positive North), and the $\hat{\mathbf{y}}$ axis completes the orthogonal right-handed frame. The IMF is represented by the yellow curve, with its tangent vector $\mathbf{B}$ in blue. Panel (**b**): the MEMFA reference frame. The $\hat{\boldsymbol{\mu}}$ axis is aligned to the main ambient magnetic field, the $\hat{\boldsymbol{\phi}}$ axis is aligned to the main electric field, and the $\hat{v}$ axis completes the orthogonal right-handed frame. The yellow curve represents the IMF, that not necessarily lies in the ecliptic plane at the Earth's orbit. This implies that the IEF also has a component in the ecliptic plane. The solar wind velocity vector is pictured in green.

2.1. The MEMFA Referece Frame Definitions and Rotation Procedure

This section describes the rotation procedure from the HEE coordinate system to the MEMFA (Mean ElectroMagnetic Fields Aligned) coordinate system. Without losing generality, we refer to the HEE as the starting reference frame hereafter. To define the MEMFA reference frame, we need to know the characteristic time scale, which is indicated as T_S, to separate the main magnetic field from its smaller period variations. With this assumption of time scale separation, the magnetic field can be thought of as a sum of a long period ambient magnetic field $\mathbf{B_0}(t)$, a short period (high frequency) perturbation term $\mathbf{b}(t)$ and an incoherent noise $\mathbf{n_b}(t)$:

$$\mathbf{B}(t) = \mathbf{B_0}(t) + \mathbf{b}(t) + \mathbf{n_b}(t) \tag{2}$$

In Equation (2), $\mathbf{B_0}$ corresponds to the mean IMF.

As for $\mathbf{B_0}$, also $\mathbf{V_0}$ represents the long period component of the solar wind velocity; following the previous definition for $\mathbf{B}$, it follows that

$$\mathbf{V}(t) = \mathbf{V_0}(t) + \mathbf{v}(t) + \mathbf{n_v}(t) \tag{3}$$

where, $\mathbf{v}(t)$ represents the velocity perturbation term and $\mathbf{n_v}(t)$ the incoherent noise.

The MEMFA coordinate system has the $\hat{\boldsymbol{\mu}}$ axis aligned to the main ambient magnetic field, the $\hat{\boldsymbol{\phi}}$ axis aligned to the main electric field ($\mathbf{E_0}(t) = -\mathbf{V_0}(t) \times \mathbf{B_0}(t)$), and the $\hat{v}$ axis that completes the orthogonal right-handed frame ($\hat{v} = \hat{\boldsymbol{\mu}} \times \hat{\boldsymbol{\phi}}$). The MEMFA unit vectors are therefore defined as follows:

$$\hat{\boldsymbol{\mu}}(t) = \frac{\mathbf{B_0}(t)}{\| \mathbf{B_0}(t) \|} \tag{4}$$

$$\hat{\boldsymbol{\phi}}(t) = \frac{\mathbf{B_0}(t) \times \mathbf{V_0}(t)}{||\mathbf{B_0}(t) \times \mathbf{V_0}(t)||} \tag{5}$$

$$\hat{v}(t) = \hat{\boldsymbol{\mu}}(t) \times \hat{\boldsymbol{\phi}}(t) \tag{6}$$

so that the instantaneous rotation matrix from HEE to the MEMFA reference frame can be computed:

$$\mathbf{R}(t) = \begin{bmatrix} \hat{\mu_x}(t) & \hat{\mu_y}(t) & \hat{\mu_z}(t) \\ \hat{\phi_x}(t) & \hat{\phi_y}(t) & \hat{\phi_z}(t) \\ \hat{\nu_x}(t) & \hat{\nu_y}(t) & \hat{\nu_z}(t) \end{bmatrix} \tag{7}$$

allowing us to define any vector in the new MEMFA reference frame.

Obviously, once we compute the rotation matrix from HEE to the MEMFA coordinate system, based on the magnetic field time scale separation, we can use the same $R(t)$ to rotate other vectors from HEE to the MEMFA reference frame, such as the velocity vector $\mathbf{V}$. By these definitions, it follows that both velocity and magnetic field vectors can be rotated as follows:

$$\mathbf{B}(t)^{'} = \mathbf{R}(t)\mathbf{B}(t) \tag{8}$$

$$\mathbf{V}(t)^{'} = \mathbf{R}(t)\mathbf{V}(t) \tag{9}$$

where, $\mathbf{R}(t)$ is the rotation matrix, the vectors with the apex on the left-hand side of the Equations (8) and (9) refer to the MEMFA reference frame and the vectors without apex on the right-hand refer to the HEE reference frame.

The MEMFA reference frame gives us information about the direction of the main magnetic field (first direction), and the second direction ($\hat{\boldsymbol{\phi}}$) gives us information about the main electric field direction. As we will see later, these quantities are important because they help us to identify the fluctuations in the SW plasma, but they can also have other applications, such as in the proximity of the magnetosphere.

Since SW Alfvén waves manifest non-linear behavior, the time scale separation is performed by the EMD method, introduced by [38] to analyze non-linear and non-stationary signals (e.g., [33,39,40]). The EMD is a sifting procedure-based technique able to adaptively decompose a multiscale signal into a sum of a finite number of roughly zero mean oscillating components called Intrinsic Mode Functions, and a residue. Those functions form a complete and nearly orthogonal basis, and they are identified without leaving the time domain (they have the same length as the original signal), thus preserving the varying frequencies. In this work, we are interested in applying the rotation procedure to a corotating high-speed SW stream, in order to separate its main magnetic field structure from the fluctuation within it. Clearly, physical phenomena do not change with the change in the reference system; nonetheless, a properly defined reference frame, based on the physical quantities involved, allows us to better understand the physics that occur.

Previous studies [8,34] showed that Alfvénic fluctuations typically have periods ranging between a few minutes and a few hours. To efficiently take into account this timescale separation in the MEMFA rotation procedure, we choose a time window of 6 h. This time window is wide enough to include all Alfvénic fluctuations therein, but, at the same time, not too wide to follow the variability of the typical ambient field in a corotating stream.

Then, we assume as ambient magnetic field $\mathbf{B_0}(t)$ all variation with a time scale greater than $T_S = 6$ h (frequencies lower than 0.005 mHz), and consequently, we consider magnetic field fluctuations all variations $\mathbf{b}(t)$ with a time scale lower than T_S (frequencies greater than 0.005 mHz), compatible with what was stated in the introduction.

2.1.1. White Noise + Localized Alfvén Waves

This section shows how the procedure works when applied to a simulated corotating SW stream with localized Alfvén waves and white noise. The basic idea is to understand if the proposed procedure is able to separate Alfvén waves from the ambient signals and project these waves in the orthogonal plane to the main field. To test this procedure, a good starting point is to create a synthetic corotating stream in the HEE reference frame, which is the reference system where we usually have the data. Then, we can apply the rotation procedure by computing the instantaneous rotation matrix $\mathbf{R_1}(t)$ from HEE to the MEMFA coordinate system, in order to add the Alfvén waves to signals in the latter

reference frame. As mentioned in the introduction, Alfvén waves propagate along the main magnetic field direction, with magnetic and velocity perturbations in the plane orthogonal to the main ambient field. In the MEMFA reference frame, we identify the main field direction, that is the $\hat{\boldsymbol{\mu}}$ one. Therefore, in this frame, we can easily introduce Alfvén waves, seen as perturbations to the main signal, in both velocity and magnetic field components orthogonal to the $\hat{\boldsymbol{\mu}}$ direction. In this test, we chose to add Alfvén waves in the $\hat{\boldsymbol{\phi}}$ direction, without losing generality. Of course, the adding waves, to be Alfvénic, must comply with other conditions, that are the magnetic and velocity energy equipartition, and no phase difference between magnetic and velocity perturbations. In a general sense, we can easily write the in-phase magnetic and velocity perturbations as

$$b_\phi = A_B(t)cos(2\pi f(t)t) \tag{10}$$

$$v_\phi = A_V(t)cos(2\pi f(t)t) \tag{11}$$

where $A_B(t)$ and $A_V(t)$ are the fluctuations amplitudes for both magnetic and velocity $\hat{\boldsymbol{\phi}}$ component. These amplitudes are linked by the equipartition of magnetic and kinetic energy:

$$\frac{{b_\phi}^2}{2\mu_0} = \frac{1}{2} n m_p {v_\phi}^2 \tag{12}$$

as expected for an Alfvèn wave. Since the signal's energy is proportional to its amplitude, we defined the amplitude of the magnetic fluctuation to 1 nT, which is in accordance with real data by observing several SW corotating structures (not shown here); in this regard, we calculated the amplitude of the kinetic fluctuation accordingly, through an appropriate multiplicative constant $1/\sqrt{\mu_0 n m_p}$, where $\mu_0 = 4\pi \times 10^{-7}$ H/m is the permeability constant, n is the plasma density (here measured in counts/cm^3), and $m_p = 1.67 \times 10^{-27}$ kg is the proton mass. The frequency $f(t)$ varies in the range 0.05–3 mHz, which are values well in accordance with those of typical Alfvén ULF waves in the SW at 1 AU, from tens to hundredths of mHz [8]. Then, both amplitudes are modulated by a window, i.e., a weight function or taper that smoothly goes to zero at the end points of the time series. Specifically, we use a Tukey window, whose weights are defined by a unitary amplitude cosine function at the edges of the time series, in order to restrict the fluctuations only in the HSS region and the beginning of the RR. This choice is a consequence of the well-known Alfvénic character of SW corotating streams, typically most Alfvénic in the high-speed plateau [4,8,37,41], as mentioned in the introduction.

Once we add Alfvén waves in the MEMFA coordinate system, we use the inverse of the previous rotation matrix to come back to the HEE reference frame, via $\mathbf{R_1}(t)^{-1}$. Then, in the HEE reference system, we add a white noise, which corresponds to a random signal having equal intensity at different frequencies, calculated according to experimental observations in the HEE reference system. At this point, we have magnetic and velocity components in HEE coordinate system containing Alfvén waves and noise, as a real case has. Starting from this, in order to check if the procedure is able to recognize Alfvén waves in noisy signals without loss of information, we newly apply the rotation procedure from HEE to MEMFA. This was accomplished by computing a new instantaneous rotation matrix $\mathbf{R_2}(t)$. If we find the Alfvénic fluctuations (previously inserted), it means that the procedure is able to well identify them.

We can outline the performance of the procedure as follows:

1. Identify or define velocity and magnetic field components profiles in the HEE coordinate system.
2. Apply the rotation procedure from the HEE to MEMFA coordinate system, using the instantaneous rotation matrix $\mathbf{R_1}(t)$.
3. In the MEMFA reference frame, we can easily add the Alfvén waves (with $\mathbf{k} \parallel \mathbf{B_0}$ where $\mathbf{k}$ is the wave vector).

4. Use the inverse of the previous rotation matrix, $\mathbf{R_1}(t)^{-1}$, to come back in the HEE reference frame, knowing that there are Alfvén waves in the signals.
5. Add the noise to each component, of both **V** and **B**. Now we have velocity and magnetic field components within Alfvén waves and noise in the HEE reference frame.
6. Apply a new rotation procedure from the HEE to MEMFA coordinate system, using the instantaneous rotation matrix $\mathbf{R_2}(t)$ and check if this procedure is able to identify Alfvén waves embedded in signals in the presence of noise.

We point out that the methodology and the procedure used in this work do not operate in the frequency domain, therefore the shift Doppler does not affect our results.

Figure 3 shows the analytic profiles of the SW magnetic field (panel a) and velocity (panel b) of a typical corotating stream, as seen in an HEE reference system. A corotating SW stream, as previously shown in Figure 1, is characterized by a CIR where the compression occurs, with a consequent increase in plasma density and magnetic field intensity; then follows a high-velocity plateau, in the so-called HSS region, where the plasma density and the magnetic field intensity decrease; then the RR occurs, characterized by a velocity decrease. The synthetic profiles are reproduced to be representative of a typical real corotating stream. The vertical dashed pink line refers to the transition from the CIR to the HSS region of the simulated corotating stream. The vertical dashed green line refers to the transition from the HSS region to the RR. After the first rotation procedure, via $\mathbf{R_1}(t)$, $\mathbf{V_0}$ and $\mathbf{B_0}$ are rotated in the MEMFA reference frame, as shown in Figure 3c,d. The instantaneous rotation matrix $\mathbf{R_1}(t)$ is computed based on the magnetic field cut-off time of 6 h, as explained in Section 2.1.

As shown in Figure 3c, the main magnetic field $B_{0\mu}$ component (in blue) is very well identified by the procedure, while the other two magnetic field components $B_{0\phi}$ and $B_{0\nu}$, in the absence of perturbations, are null. The velocity components in the MEMFA reference frame, which are computed with the same rotation matrix $\mathbf{R_1}(t)$, are shown in the bottom panel of the same figure. Since the second unit vector $\hat{\boldsymbol{\phi}}(t)$ of the MEMFA system is calculated as in Equation (5), the $V_{0\phi}$ component (in red), in the absence of perturbation, is null because $V_{0\phi}$ is perpendicular to $\mathbf{V_0}$. At this point, being in a reference system aligned to the main field, we add Alfvén ULF waves in the $\hat{\boldsymbol{\phi}}$ direction, orthogonal to it.

The MEMFA magnetic and velocity components, along with Alfvén waves, are shown in Figure 4a,b. At this point, the signal contains its main trend and Alfvén ULF waves, but not yet the noise. Because we can have information, from real data, about typical noise amplitude values in the HEE reference frame, we can apply the inversion rotation matrix $\mathbf{R_1}^{-1}(t)$ and come back in the HEE reference system, where we can add noise to make the simulation more realistic. In this section, we reproduce white noise for both magnetic field and velocity components, which has an amplitude that is calculated from the standard deviations of real values fluctuations. The latter quantities were estimated by removing the main trend from real data, so they contain both waves and noise.

Figure 5 shows the new rotated magnetic (panel c) and velocity components (panel d) in the MEMFA reference frame, via the new instantaneous rotation matrix $\mathbf{R_2}(t)$. After the rotation (via $\mathbf{R_2}(t)$), the noise remains in all components, while Alfvén waves are found only in the $\hat{\boldsymbol{\phi}}$ direction, confirming the proper functioning of the procedure (see also Figure 5e that is a magnification example of the magnetic field fluctuations). Further confirmation of the previous statement will be shown in Section 2.2. Panels a and b show an example of magnetic (top panel) and velocity components (bottom panel) with Alfvénic fluctuations (in the HSS and the beginning of the RR) and white noise embedded in the entire stream, in the HEE reference frame. This can be considered as the equivalent starting point of real data studies because when we deal with satellite data, they can generally be seen as the superposition of a main trend, some typical signals, and noise. At this point, we can apply the rotation procedure from scratch, finding a new instantaneous rotation matrix $\mathbf{R_2}(t)$; then, we check if the procedure can recognize not only the correct separation of the three magnetic and velocity components, but also the identification of the Alfvén waves only in the $\hat{\boldsymbol{\phi}}$ direction, as previously inserted.

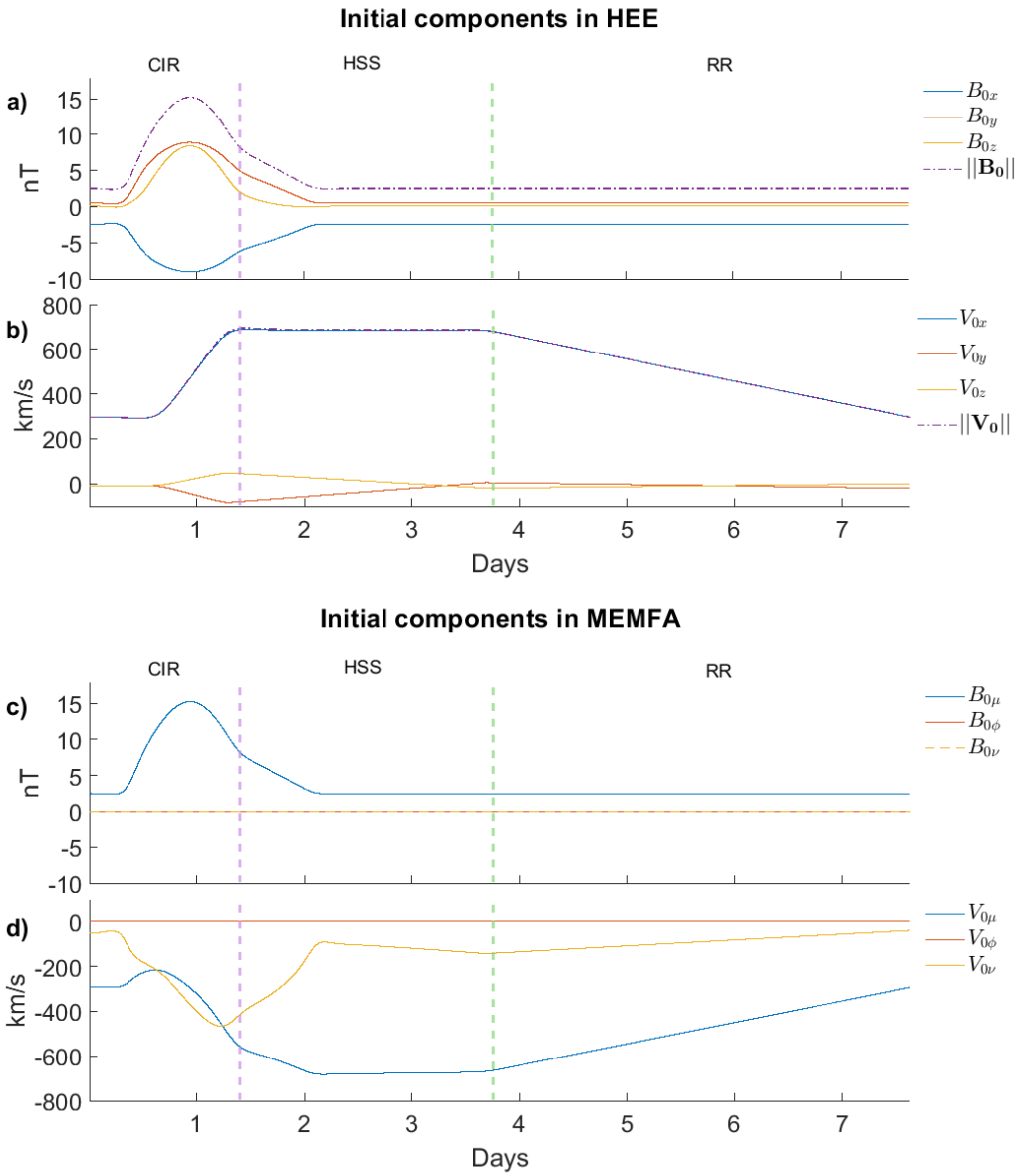

Figure 3. Synthetic profiles of magnetic field (panel **a**) and velocity (panel **b**) components used to recreate a corotating SW stream in the HEE reference frame. Synthetic profiles of magnetic field (panel **c**) and velocity (panel **d**) components in the MEMFA reference frame, obtained by the rotation procedure from HEE to MEMFA via $\mathbf{R_1}(t)$. The x-axis refers to days in a simulated case. The vertical dashed pink line refers to the transition from the CIR to the HSS region of the simulated corotating stream. The vertical dashed green line refers to the transition from the HSS region to the RR of the simulated corotating stream.

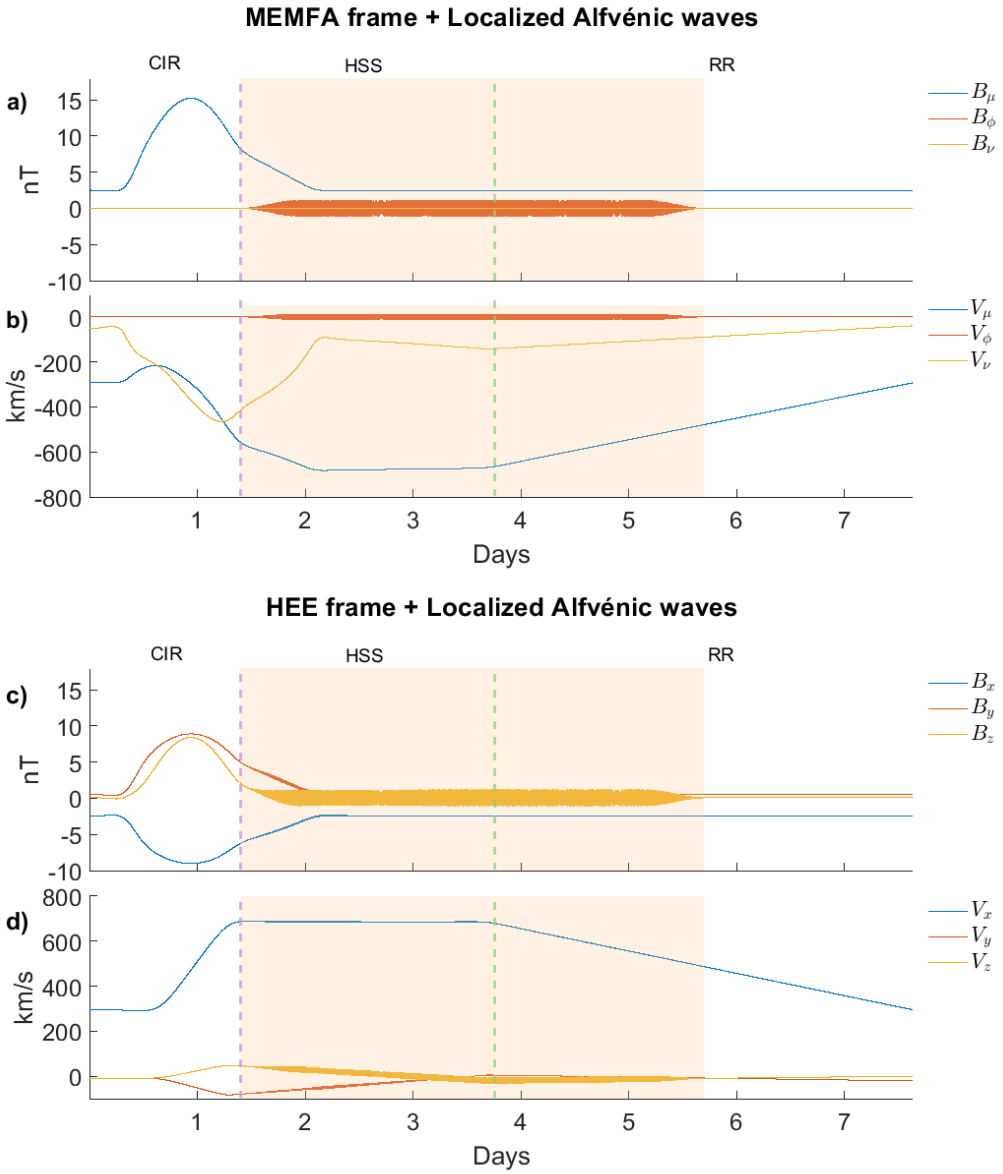

Figure 4. Magnetic field (panel **a**) and velocity (panel **b**) MEMFA components with the addition of Alfvén waves in the HSS region and at the beginning of RR. Magnetic field (panel **c**) and velocity (panel **d**) HEE components, containing Alfvén waves, obtained by the use of the inverse rotation matrix $\mathbf{R_1}^{-1}(t)$. The x-axis refers to days in a simulated case. The vertical dashed pink line refers to the transition from the CIR to the HSS region of the simulated corotating stream. The vertical dashed green line refers to the transition from the HSS region to the RR of the simulated corotating stream. The shaded region refers to the one with the synthetic Alfvén waves.

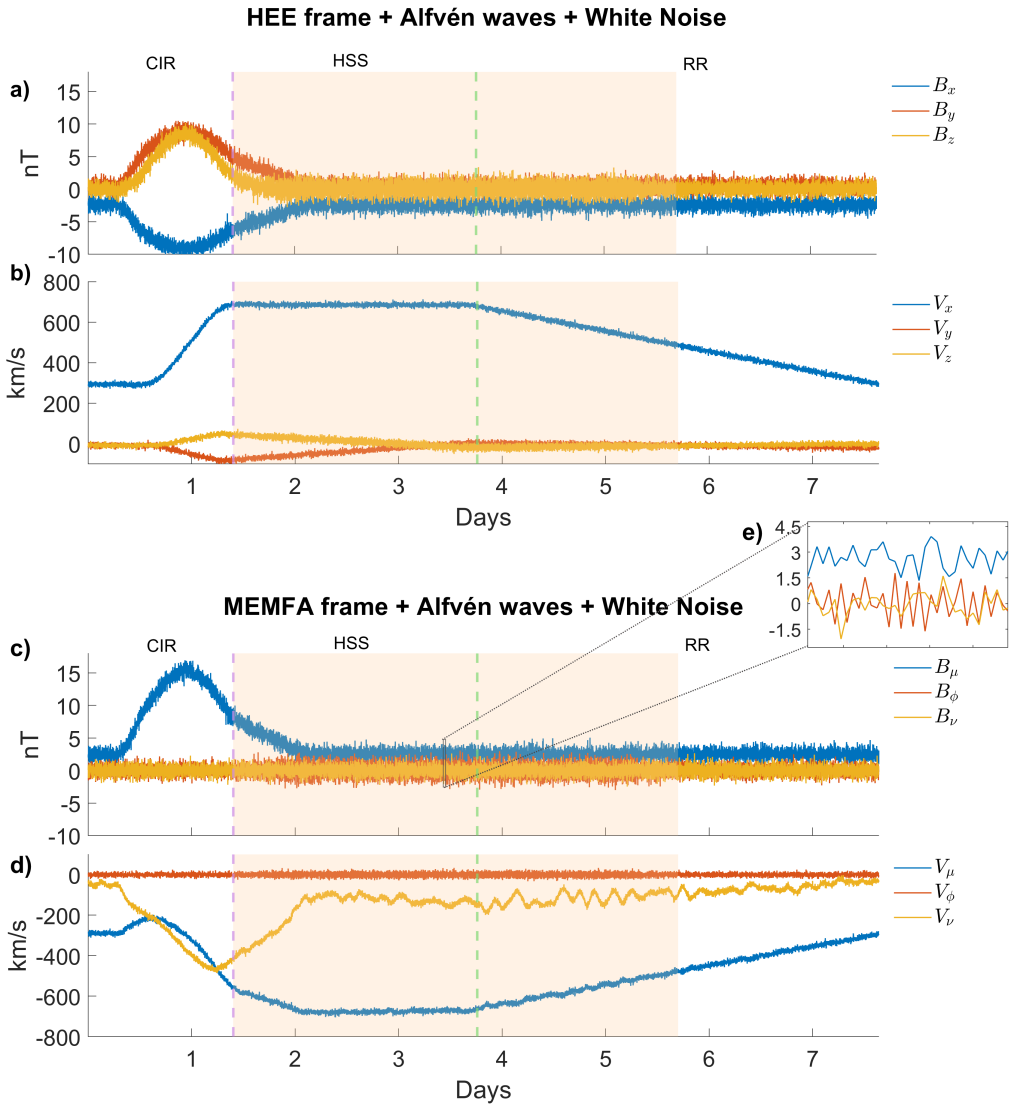

Figure 5. Magnetic field (panel **a**) and velocity (panel **b**) HEE components, containing Alfvén waves, with the addition of white noise. Magnetic field (panel **c**) and velocity (panel **d**) MEMFA components, obtained by a new rotation procedure from HEE to MEMFA via $\mathbf{R_2}(t)$, starting from the velocity and magnetic field HEE components containing Alfvén waves and white noise. A magnification of magnetic field fluctuations in the MEMFA reference frame is reported in (panel **e**) as an example. The x-axis refers to days in a simulated case. The vertical dashed pink line refers to the transition from the CIR to the HSS region of the simulated corotating stream. The vertical dashed green line refers to the transition from the HSS region to the RR of the simulated corotating stream. The shaded region refers to the one with the synthetic Alfvén waves.

2.1.2. Red Noise + Localized Alfvén Waves

Both velocity and magnetic field in the SW are characterized by colored noise, which is a non-flat frequency spectrum. To reproduce a noise as similar as possible to the real noise embedded in the SW, we reproduce a red noise [42] with a first-order auto-regressive process (AR1) obtained from the auto-correlation at $lag = 1$ of both magnetic and velocity components of a real case study.

In this section, we repeated the test, as seen in the previous section, no longer in the presence of white noise but in the presence of red noise computed as just mentioned. The points from 1 to 4 of the outline test procedure mentioned in Section 2.1.1 remain the same; hereafter, we change the kind of noise we added in point 5. Figure 6a,b shows

magnetic and velocity components in the HEE reference frame with the red noise embedded within them. As said for the white noise, this can be considered as the equivalent starting point of a real data series, formed by a main trend with added signals, and red noise typical of both magnetic and velocity components. The rotation procedure can be repeated through a new instantaneous rotation matrix $\mathbf{R_2}(t)$, obtaining the MEMFA magnetic and velocity components shown in Figure 6c,d, respectively. Also in this case, after the rotation, the noise remains in all the components, while the Alfvénic fluctuations are detected only in the $\hat{\boldsymbol{\phi}}$ component of both the magnetic field and velocity (see also Figure 6e, which is a magnification example of the magnetic field fluctuations). The previous statement will be confirmed further in Section 2.2, Figure 8.

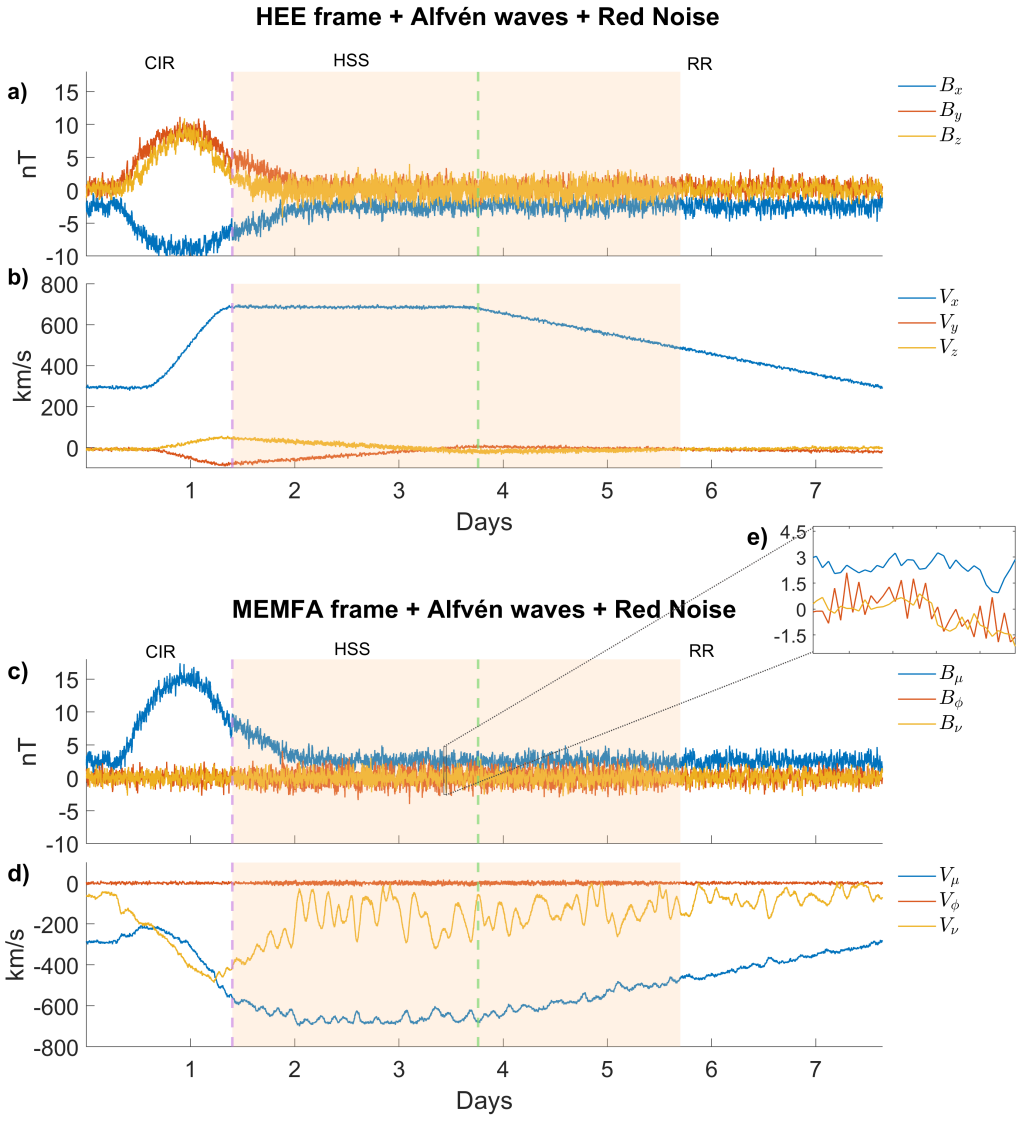

Figure 6. Magnetic field (panel **a**) and velocity (panel **b**) HEE components, containing Alfvén waves, with the addition of red noise. Magnetic field (panel **c**) and velocity (panel **d**) MEMFA components, obtained by a new rotation procedure from HEE to MEMFA via $\mathbf{R_2}(t)$, starting from the velocity and magnetic field HEE components containing Alfvén waves and red noise. A magnification of magnetic field fluctuations in the MEMFA reference frame is reported in (panel **e**) as an example. The *x*-axis refers to days in a simulated case. The vertical dashed pink line refers to the transition from the CIR to the HSS region of the simulated corotating stream. The vertical dashed green line refers to the transition from the HSS region to the RR of the simulated corotating stream. The shaded region is the one containing Alfvén ULF waves.

2.2. Monte Carlo Test and Reliability

To check the reliability of the procedure, we made a MC test by generating surrogates of both white and red noise, with different amplitudes, in order to compute the Signal-to-Noise Ratio (SNR_A) in terms of amplitude. Then, we calculated the correlation coefficient between the MEMFA components (obtained via $\mathbf{R_1}(t)$ matrix) with only the localized Alfvén waves and the MEMFA components (obtained via $\mathbf{R_2}(t)$ matrix) in the presence of both localized Alfvén waves and noise.

The SNR_A is the ratio between the signal amplitude and the noise amplitude, therefore it gives us an idea of how much the signal prevails over the noise and vice versa. In the MC test, we decided to vary the noise amplitudes in order to vary the SNR_A. We defined the amplitudes of the noise of both magnetic field and velocity as $N_B = A_N\sigma_B$ and $N_V = A_N\sigma_V/C$ where A_N is the varying dimensionless amplitude, σ_B and σ_V are the standard deviations of real values fluctuations (obtained by removing the main trend), and C (see Equation (14)) is a dimensionless multiplicative constant that links the amplitude of the magnetic noise with that of the velocity noise, while maintaining the uncorrelated noise between them, in the case of white noise. By imposing equality between the

$$SNR_A(B) = \frac{A_B}{N_B} = \frac{A_B}{A_N\sigma_B} \quad , \quad SNR_A(V) = \frac{A_V}{N_V} = \frac{A_v}{A_N\sigma_V/C} \tag{13}$$

We can find the proportionality constant between noise amplitudes:

$$C = \frac{A_B\sigma_V}{A_V\sigma_B} \tag{14}$$

Figure 7 shows the correlation coefficient computed between each MEMFA component with only localized Alfvén waves in the absence of noise and the homonym MEMFA component in the presence of both Alfvén waves and white noise. Recall that, in the test procedure, the Alfvén wave was added only in the $\hat{\boldsymbol{\phi}}$ component, orthogonal to that ($\hat{\boldsymbol{\mu}}$) aligned with the ambient magnetic field. Each panel shows the mean correlation trend computed by averaging over 40 surrogates at each fixed SNR_A (colored dots) and its confidence interval at 95% (shaded area). In addition, for each SNR_A, we computed the corresponding average correlation r_{mean}. We can see that these correlations computed between $\hat{\boldsymbol{\mu}}$ and $\hat{\boldsymbol{v}}$ components, of both magnetic field and velocity, are zero, whereas the correlation computed between $\boldsymbol{B_\phi}$ (obtained via $\mathbf{R_1}(t)$) with only Alfvén waves and $\boldsymbol{B_\phi}$ (obtained via $\mathbf{R_2}(t)$) with Alfvén waves and white noise, reach a value of $r = 0.7$ in correspondence with $SNR_A = 2.04$ for both the magnetic and the velocity component; it means that the signal (total signal-noise) in terms of amplitude is greater than $2/3$ ($\sim 66\%$) of the total signal.

Figure 8 shows the correlation coefficient computed between each MEMFA component with only localized Alfvén waves in the absence of noise and the homonym MEMFA component in the presence of both Alfvén waves and red noise. For each magnetic and velocity component, the red noise was computed with an auto-regressive coefficient obtained from real data, respectively. Again, in the presence of red noise, the correlation coefficient is basically zero for components that do not contain ULF waves, and it grows rapidly towards 1 for the $\hat{\boldsymbol{\phi}}$ component, where we have previously added ULF Alfvén waves, which are well found back after the second rotation procedure.

The correlation computed between $\boldsymbol{B_\phi}$ (obtained via $\mathbf{R_1}(t)$) with only Alfvén waves and $\boldsymbol{B_\phi}$ (obtained via $\mathbf{R_2}(t)$) with Alfvén waves and red noise, reaches a value of $r = 0.7$ in correspondence with $SNR_A = 4.1$ and $SNR_A = 3.7$ for the magnetic and velocity components, respectively; it means that if we approximate $SNR_A = 4$ for both components, the signal (total signal – noise) in terms of amplitude is greater than $4/5$ ($\sim 80\%$) of the total signal for both the magnetic and velocity $\hat{\boldsymbol{\phi}}$ components. In both cases, the procedure is able to recognize the Alfvénic fluctuations in the presence of white noise and red noise. Furthermore, the procedure is able to identify the main component's profiles, giving a

high correlation value for all three components of both magnetic field and velocity (not shown here). We want to stress that the ULF fluctuation that was only present in the $\hat{\boldsymbol{\phi}}$ component is found, after the second rotation, only in the same $\hat{\boldsymbol{\phi}}$ component and not in the other components.

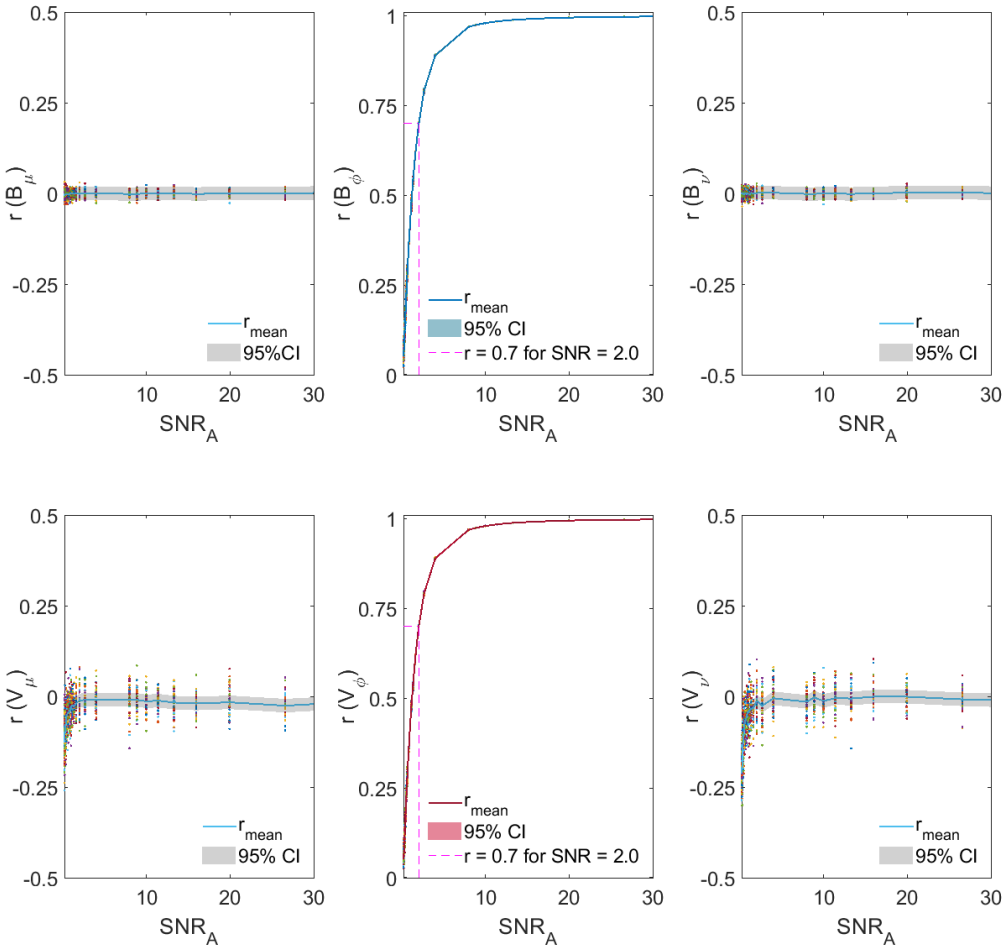

Figure 7. Correlation coefficient computed between each MEMFA component with only localized Alfvén waves in the absence of noise and the homonym MEMFA component in the presence of both Alfvén waves and white noise (dots). The **first** row shows the correlation coefficient related to the three magnetic field components computed for different SNR_A values, where SNR_A is the Signal-to-Noise Ratio evaluated with the Amplitudes of signals and noise. The **second** row shows the correlation coefficient related to the three velocity components computed for different SNR_A values. r_{mean} refers to the average correlation coefficient, while CI refers to the Confidence Interval, shown at 95%. Only for the $\hat{\phi}$ component, we reported the extrapolated SNR_A in correspondence to a correlation value of $r = 0.7$ (pink dashed lines).

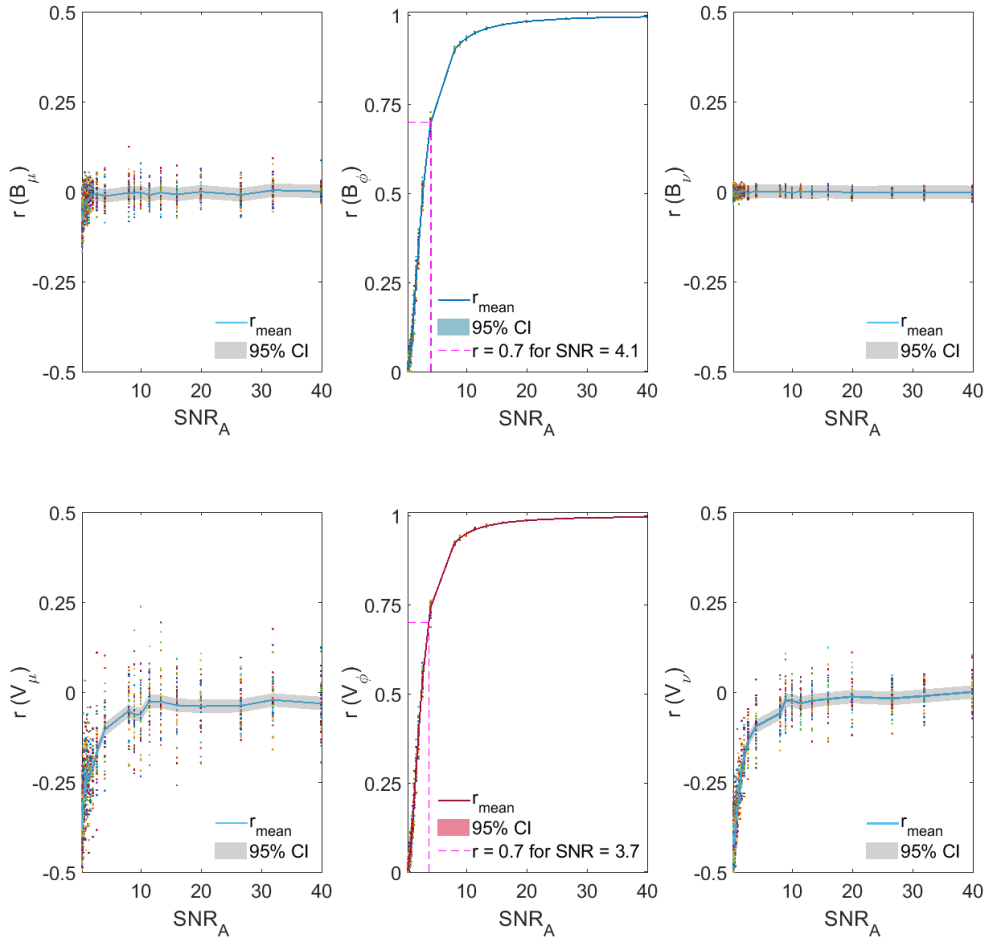

Figure 8. Correlation coefficient computed between each MEMFA component with only localized Alfvén waves in the absence of noise and the homonym MEMFA component in the presence of both Alfvén waves and red noise (dots). The **first** row shows the correlation coefficient related to the three magnetic field components computed for different SNR_A values, where SNR_A is the Signal-to-Noise Ratio evaluated with the Amplitudes of signals and noise. The **second** row shows the correlation coefficient related to the three velocity components computed for different SNR_A values. r_{mean} refers to the average correlation coefficient, while CI refers to the Confidence Interval, shown at 95%. Only for the $\hat{\phi}$ component, we reported the extrapolated SNR_A in correspondence to a correlation value of $r = 0.7$ (pink dashed lines).

3. Results of the Applied Procedure on Simulated and Real Case Study

To study the Alfvénicity in the inertial range in the SW turbulence, adiabatic invariants are widely used, like the normalized cross helicity σ_c and the normalized residual energy σ_r ([26] and references therein):

$$\sigma_c = \frac{e^+ - e^-}{e^+ + e^-} \tag{15}$$

$$\sigma_r = \frac{e^v - e^b}{e^v + e^b} \tag{16}$$

where e^+ and e^- are the variances related to Elsässer variables $\mathbf{z}^+$ and $\mathbf{z}^-$, whereas e^v is the velocity variance and e^b is the magnetic field variance in Alfvén units. For a pure Alfvén wave we expect $\sigma_r \to 0$ and $\sigma_c \to \pm 1$.

3.1. Application to Syntetic Data

Therefore, to check the Alfvénicity in our cases, we computed these quantities both in the absence and in the presence of Alfvén waves. In the absence of Alfvén waves (see red and blue dashed curves in panel a of Figure 9) $\sigma_c \to 0$ and $\sigma_r \to 1$ as expected for a compressional wave. When Alfvén waves, localized in the shaded region, are added, there is the opposite scenario: $\sigma_c \to 1$ and $\sigma_r \to 0$ as expected for Alfvén waves.

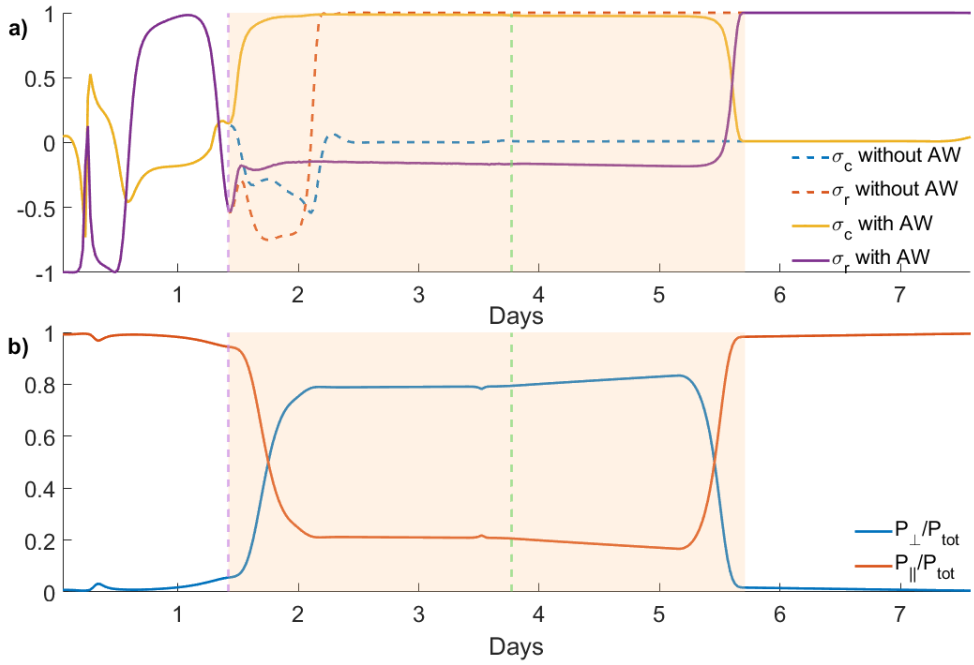

Figure 9. Panel (**a**) shows the normalized cross helicity σ_c and the normalized residual energy σ_r computed in the absence of Alfvén waves (AW) (dashed lines) and the same quantities computed in the presence of AW (solid line). Panel (**b**) shows the normalized power $P_{\parallel}$ aligned to the main magnetic field and the one orthogonal to it $P_{\perp}$. The vertical dashed pink line refers to the transition from the CIR to the HSS region of the simulated corotating stream. The vertical dashed green line refers to the transition from the HSS region to the RR. The shaded region is the one containing Alfvén ULF waves.

The behavior of these variables in the compressive region is due to the wide variability of the stream in this region. Indeed, while for a purely Alfvén wave in a homogeneous plasma, the method using Elsässer variables is strictly valid, for a compressible and inhomogeneous plasma pure MHD waves are no longer normal modes, but the waves become coupled or show mixed nature between the Alfvénic and the magnetosonic one. In this case, magnetosonic waves are described by both z+ and z-, and cannot be separated inward and outward from the background field [43].

In our test, we can compute two quantities that we can compare with σ_c and σ_r to obtain more information about the characteristics of fluctuations. We performed the spectral analysis of both magnetic and velocity components in the MEMFA reference frame, to define the normalized power related to the two main directions: the one aligned and the one orthogonal to the main ambient field. Obviously, power is a scalar quantity, hence subscriptions $\parallel$ and $\perp$ refer to the components used to calculate the power itself. We define $P_{\perp} = P_{V_{\perp}} + P_{B_{\perp}|_V}$ where $P_{V_{\perp}}$ is the sum of powers of V_{ϕ} and V_{ν}, and $P_{B_{\perp}|_V}$ is the sum of powers of B_{ϕ} and B_{ν} both re-scaled to velocity dimensions. At the same way, we define $P_{\parallel} = P_{V_{\parallel}} + P_{B_{\parallel}|V}$ where $P_{V_{\parallel}}$ is the power of V_{μ} and $P_{B_{\parallel}|V}$ is the power of B_{μ} re-scaled to velocity dimensions. Alfvén waves are characterized by perturbation in the direction orthogonal to the main field, therefore we expect a prevalence of $P_{\perp}$ in their presence.

In panel b of Figure 9 are shown $P_{\perp}/P_{Tot}$ in blue and $P_{\parallel}/P_{Tot}$ in red (where P_{Tot} is the total power), both defined in the range $[0, 1]$. In the shaded region, which corresponds to

the one with Alfvén waves, $P_{\perp}/P_{Tot}$ is greater than $P_{\parallel}/P_{Tot}$, as expected. There is a well-founded correspondence ($r = 0.95$) between σ_c and $P_{\perp}/P_{Tot}$ and also ($r = 0.88$) between σ_r and $P_{\parallel}/P_{Tot}$, in the MEMFA reference frame.

3.2. Application to Real Event

We applied the same procedure to a real event, for a high-velocity stream from 9 to 15 August 2008 (solar minimum activity).

Figure 10 shows the results (smoothed over 36 h) obtained with the procedure applied to the real case study. In the top panel are plotted the normalized cross helicity σ_c (in blue) and the normalized SW power $P_{\perp}/P_{Tot}$ (in yellow) orthogonal to the main field. In the middle panel are plotted the normalized residual energy σ_r (in green) changed in sign and the normalized SW power $P_{\parallel}/P_{Tot}$ (in red) aligned to the main field. In the bottom panel is shown the moving correlations (over 48 h) between the two quantities (σ_c and $P_{\perp}/P_{Tot}$) shown in the top panel (in yellow) and between the two quantities (σ_r and $P_{\parallel}/P_{Tot}$) shown in the middle panel (in red). The correlation gives us an idea of how well the two procedures are in agreement with each other. From the beginning of DoY 223 to the end of DoY 225, we observe that both correlations have similar trends and both correlations have almost high values (except for a quick decrease at the beginning of DoY 224). These results suggest a good accordance between the two methods used. After DoY 226, the correlations decrease, suggesting that the two methods give different information. When there is accordance between the two methods and σ_c and $P_{\perp}/P_{Tot}$ reach high values, we are confident there are Alfvén waves. When there is still accordance between the two methods and σ_c and $P_{\perp}/P_{Tot}$ values are low, we are confident that there are no Alfvén waves. When the two methods are not in agreement, there could be the presence of isotropic waves also in the orthogonal direction.

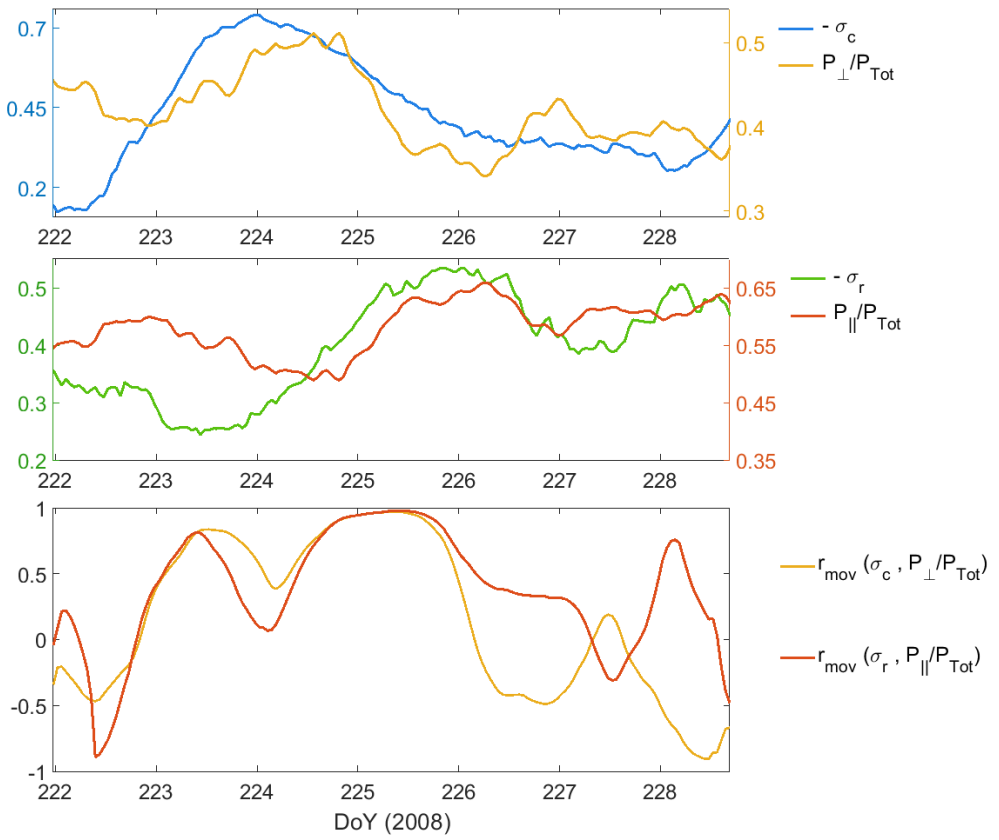

Figure 10. Top panel: smoothed $-\sigma_c$ in blue and $P_{\perp}/P_{Tot}$ in yellow. **Middle** panel: smoothed $-\sigma_r$ in green and $P_{\parallel}/P_{Tot}$ in red. **Bottom** panel: moving correlation (r_{mov}) between $-\sigma_c$ and $P_{\perp}/P_{Tot}$ in yellow, and moving correlation between $-\sigma_r$ and $P_{\parallel}/P_{Tot}$ in red.

4. Discussion and Conclusions

We described a new method that allows us to define an inertial rotated reference frame aligned to both the main magnetic and electric field, where we can easily identify Alfvén waves, also in the presence of noise. This method is easily adaptable to a general context. Previously, investigations in the SW were conducted by [33], regarding long-lasting upstream waves. In their study, the authors showed that the wave energy conservation from the original geocentric reference frame to the MFA reference frame was satisfied as expected for a rotation procedure, by using a specific EMD-based algorithm. It is well known that the SW more efficiently transfers its energy to the Earth system during time intervals characterized by IMF–magnetosphere coupling, due to negative values of the B_z component of the IMF, which in turn corresponds to a down-dusk IEF component.

High-Intensity, Long-Duration, Continuous AE Activity (HILDCAA) events seem to be related to HSS, to the Alfvénic fluctuations therein, and to the long-lasting B_z fluctuations in the corotating SW streams; those waves are able to modulate geomagnetic activity as investigated by [21,22,35,44]. The geomagnetic activity enhancements, also occurring during those events, also affect the ionosphere, thermosphere, and atmosphere parameters, as reported in many works (e.g., [45–49]). Therefore, it is important to study the SW origin of the geomagnetic activity enhancements related to the SW corotating streams for a better study of the Sun–Earth interactions.

In this work, we improved the over-mentioned EMD rotation procedure by also considering the main IEF direction; the constraint to this second direction led us to the MEMFA reference frame. In this context, the procedure here proposed easily allows us to simulate waves with specific characteristics, such as Alfvén waves. We also showed the capability of the MEMFA method in separating waves by selecting a reasonable time scale, in the presence of noises.

Here, we reproduce an analytic corotating SW stream profile to test the procedure and its reliability with a MC test. Based on MC test results, we notice a high correlation $(r > 0.7)$ for $SNR_A > 2.0$ for both the magnetic and the velocity component in the case of white noise; it means that the signal (total signal–noise), in terms of amplitude, is greater than 2/3 (∼66%) of the total signal. In the case of red noise, we notice as well a high correlation $(r > 0.7)$ for $SNR_A > 4.1$ for the magnetic component and for $SNR_A > 3.7$ for the velocity component; the corresponding signal percentage, in terms of amplitude, is ∼80% of the total one. The presence of red noise does not change the result much. It introduces only a small slowdown in the growth rate of the correlation of V_ϕ, which however is well recognized by the rotation procedure as the only component containing Alfvén waves. The higher extrapolated SNR_A in correspondence to the same $r = 0.7$, for the red noise case, is clearly due to the auto-regressive process of the first order (AR1), which is greater than 0 (for white noise).

This work aims to study the Alfvén waves directly in the MEMFA reference frame. To check the reliability of the proposed procedure, we compared our results with that found via the two invariants, σ_c and σ_r, computed via Elsässer variables.

We found a good correspondence between σ_c and $P_\perp / P_{Tot}$ and between σ_r and $P_\parallel / P_{Tot}$, both in the simulated case ($r(\sigma_c, P_\perp) = 0.95$ and $r(\sigma_r, P_\parallel) = 0.88$, related to HSS+RR) and in a real case study, carefully estimated by moving correlation. In the real case study, a global correlation between the two invariants and the powers in the MEMFA reference frame reaches values ~ 0.9 related to the long-term variation. The method based on the normalized cross helicity and normalized residual energy can be well-supported by the new proposed procedure, making the identification of Alfvén waves in the experimental data clearer. This aspect is particularly evident in the case study reported during the HSS region, which is the one where Alfvén waves are mostly present. A less clear correspondence between the two methods is found in the RR, possibly attributed to the filtered time series at time scales $T_S > 6$ hours required for the EMD separation in the MEMFA rotation procedure; this filter procedure was not performed in computing the two invariants. This means that during the HSS the spectral contents of the two timerange utilized to compute

the two invariants and the SW powers in the MEMFA frame are almost the same, while in the RR the two spectral contents differ.

The MEMFA reference frame can allow us to collect information not only in the main magnetic field direction but also in the main electric field one, which is the most geoeffective component in the proximity of the magnetosphere; this aspect makes the MEMFA reference frame useful in space weather investigations.

Author Contributions: Conceptualization, G.C. and M.R.; formal analysis, G.C. and M.R.; software, G.C. and M.R.; investigation, G.C. and M.R.; methodology, G.C. and M.R.; writing—original draft preparation, G.C. and M.R. All authors have read and agreed to the published version of the manuscript.

Funding: This work is supported by INGV-MUR project Pianeta Dinamico—The Working Earth (CUP D53J19000170001, law 145/2018), theme 3 SERENA (The Solar wind–Earth's magnetosphere Relationships and their Effects on ioNosphere and upper and lower Atmosphere).

Data Availability Statement: The interplanetary magnetic field and solar wind data are provided by Coordinated Data Analysis Web (CDAWeb, https://cdaweb.gsfc.nasa.gov(accessed on 21 August 2023). The EMD code was provided by G. Rilling, P. Flandrin and P. Gonçalvès at it is available at https://perso.ens-lyon.fr/patrick.flandrin/emd.html (accessed on 21 August 2023); the rednoise generator code is provided by A. Grinsted at https://www.glaciology.net/publication/2004-12-24-application-of-the-cross-wavelet-transform-and-wavelet-coherence-to-geophysical-time-series/ (accessed on 21 August 2023). The code for the MFA rotation procedure can be requested from Dr. Mauro Regi (e-mail: mauro.regi@ingv.it) or Dr. Alfredo Del Corpo (e-mail: alfredo.delcorpo@ingv.it), while the code for the MEMFA rotation procedure can be requested from Dr. Giuseppina Carnevale (e-mail: giuseppina.carnevale@ingv.it) or Dr. Mauro Regi (e-mail: mauro.regi@ingv.it).

Conflicts of Interest: The authors declare no conflict of interest.

Acronym List

The following acronyms are used in this manuscript:

AW	Alfvén Waves
CIR	Corotating Interaction Region
DoY	Day of Year
EMD	Empirical Mode Decomposition
HEE	Heliocentric Earth Ecliptic
HILDCAA	High-Intensity, Long-Duration, Continuous AE Activity
HSS	High-Speed Stream
IEF	Interplanetary Electric Field
IMF	Interplanetary Magnetic Field
MC	Monte Carlo
MEMFA	Mean ElectroMagnetic Fields Aligned
MFA	Mean Field Aligned
RN	Red Noise
RR	Rarefaction Region
SW	Solar Wind
SNR	Signa to Noise Ration
WN	White Noise

References

1. Gosling, J.; Hundhausen, A.; Bame, S. Solar wind stream evolution at large heliocentric distances: Experimental demonstration and the test of a model. *J. Geophys. Res.* **1976**, *81*, 2111–2122. [CrossRef]
2. Richardson, I.G. Solar wind stream interaction regions throughout the heliosphere. *Living Rev. Sol. Phys.* **2018**, *15*, 1. [CrossRef] [PubMed]
3. Marsch, E.; Tu, C.Y. Spectral and spatial evolution of compressible turbulence in the inner solar wind. *J. Geophys. Res. Space Phys.* **1990**, *95*, 11945–11956. [CrossRef]
4. Carnevale, G.; Bruno, R.; Marino, R.; Pietropaolo, E.; Raines, J.M. Sudden depletion of Alfvénic turbulence in the rarefaction region of corotating solar wind high-speed streams at 1 AU: Possible solar origin? *Astron. Astrophys.* **2022**, *661*, A64. [CrossRef]

5. Hundhausen, A. *Coronal Expansion and Solar Wind*; Physics and Chemistry in Space; Springer: Berlin/Heidelberg, Germany, 1972; Volume 5.
6. Coleman, P.J., Jr. Wave-like phenomena in the interplanetary plasma: Mariner 2. *Planet. Space Sci.* **1967**, *15*, 953–973. [CrossRef]
7. Coleman, P.J., Jr. Turbulence, Viscosity, and Dissipation in the Solar-Wind Plasma. *Astrophys. J.* **1968**, *153*, 371. [CrossRef]
8. Belcher, J. W.; Leverett, D., Jr. Large-amplitude Alfvén waves in the interplanetary medium, 2. *J. Geophys. Res.* **1971**, *76*, 3534–3563. [CrossRef]
9. Burlaga, L.; Turner, J. Microscale 'Alfvén waves' in the solar wind at 1 AU. *J. Geophys. Res.* **1976**, *81*, 73–77. [CrossRef]
10. Del Corpo, A.; Vellante, M.; Heilig, B.; Pietropaolo, E.; Reda, J.; Lichtenberger, J. Observing the cold plasma in the Earth's magnetosphere with the EMMA network. *Ann. Geophys.* **2019**, *62*, GM447. [CrossRef]
11. Menk, F.W.; Waters, C.L. *Magnetoseismology: Ground-Based Remote Sensing of Earth's Magnetosphere*; Wiley-VCH: Weinheim, Germany, 2013. [CrossRef]
12. Chi, P.J.; Russell, C.T. Travel-time magnetoseismology: Magnetospheric sounding by timing the tremors in space. *Geophys. Res. Lett.* **2005**, *32*, L18108. [CrossRef]
13. Takahashi, K.; Denton, R.E. Magnetospheric Mass Density as Determined by ULF Wave Analysis. *Front. Astron. Space Sci.* **2021**, *8*, 708940. [CrossRef]
14. Jones, A.; Chave, A.; Egbert, G.; Auld, D.; Bahr, K. A comparison of techniques for magnetotelluric response function estimation. *J. Geophys. Res. Solid Earth* **1989**, *94*, 201–213. [CrossRef]
15. Chave, A.D.; Jones, A.G. Introduction to the magnetotelluric method. In *The Magnetotelluric Method: Theory and Practice*; Chave, A.D., Jones, A.G., Eds.; Cambridge University Press: Cambridge, UK, 2012; pp. 1–18. [CrossRef]
16. Regi, M.; De Lauretis, M.; Francia, P. Pc5 geomagnetic fluctuations in response to solar wind excitation and their relationship with relativistic electron fluxes in the outer radiation belt. *Earth Planets Space* **2015**, *67*, 9. [CrossRef]
17. Mann, I.R.; O'Brien, T.P.; Milling, D.K. Correlations between ULF wave power, solar wind speed, and relativistic electron flux in the magnetosphere: Solar cycle dependence. *J. Atmos. Sol.-Terr. Phys.* **2004**, *66*, 187–198. [CrossRef]
18. Blum, L.W.; Halford, A.; Millan, R.; Bonnell, J.W.; Goldstein, J.; Usanova, M.; Engebretson, M.; Ohnsted, M.; Reeves, G.; Singer, H.; et al. Observations of coincident EMIC wave activity and duskside energetic electron precipitation on 18–19 January 2013. *Geophys. Res. Lett.* **2015**, *42*, 5727–5735. [CrossRef]
19. Mironova, I.A.; Aplin, K.L.; Arnold, F.; Bazilevskaya, G.A.; Harrison, R.G.; Krivolutsky, A.A.; Nicoll, K.A.; Rozanov, E.V.; Turunen, E.; Usoskin, I.G. Energetic Particle Influence on the Earth's Atmosphere. *Space Sci. Rev.* **2015**, *194*, 1–96. [CrossRef]
20. Lam, M.M.; Tinsley, B.A. Solar wind-atmospheric electricity-cloud microphysics connections to weather and climate. *J. Atmos. Sol.-Terr. Phys.* **2016**, *149*, 277–290. [CrossRef]
21. Tsurutani, B.T.; Gonzalez, W.D.; Gonzalez, A.L.C.; Tang, F.; Arballo, J.K.; Okada, M. Interplanetary origin of geomagnetic activity in the declining phase of the solar cycle. *J. Geophys. Res. Space Phys.* **1995**, *100*, 21717–21733. [CrossRef]
22. Tsurutani, B.T.; Gonzalez, W.D.; Gonzalez, A.L.C.; Guarnieri, F.L.; Gopalswamy, N.; Grande, M.; Kamide, Y.; Kasahara, Y.; Lu, G.; Mann, I.; et al. Corotating solar wind streams and recurrent geomagnetic activity: A review. *J. Geophys. Res. Space Phys.* **2006**, *111*. [CrossRef]
23. Tsurutani, B.T.; Gonzalez, W.D. The cause of high-intensity long-duration continuous AE activity (HILDCAAs): Interplanetary Alfvén wave trains. *Planet. Space Sci.* **1987**, *35*, 405–412. [CrossRef]
24. Tsurutani, B.T.; Gonzalez, W.D. The Interplanetary causes of magnetic storms: A review. *Geophys. Monogr. Ser.* **1997**, *98*, 77–89. [CrossRef]
25. Tsurutani, B.T.; Goldstein, B.E.; Smith, E.J.; Gonzalez, W.D.; Tang, F.; Akasofu, S.I.; Anderson, R.R. The interplanetary and solar causes of geomagnetic activity. *Planet. Space Sci.* **1990**, *38*, 109–126. [CrossRef]
26. Bruno, R.; Carbone, V. *Turbulence in the Solar Wind*; Springer: Berlin/Heidelberg, Germany, 2016; Volume 928. [CrossRef]
27. Clausen, L.B.N.; Yeoman, T.K.; Fear, R.C.; Behlke, R.; Lucek, E.A.; Engebretson, M.J. First simultaneous measurements of waves generated at the bow shock in the solar wind, the magnetosphere and on the ground. *Ann. Geophys.* **2009**, *27*, 357–371. [CrossRef]
28. Sarris, T.; Li, X.; Singer, H.J. A long-duration narrowband Pc5 pulsation. *J. Geophys. Res. Space Phys.* **2009**, *114*, A01213. [CrossRef]
29. Francia, P.; Regi, M.; De Lauretis, M.; Villante, U.; Pilipenko, V.A. A case study of upstream wave transmission to the ground at polar and low latitudes. *J. Geophys. Res. Space Phys.* **2012**, *117*, A01210. [CrossRef]
30. Francia, P.; De Lauretis, M.; Regi, M. ULF fluctuations observed along the SEGMA array during very low solar wind density conditions. *Planet. Space Sci.* **2013**, *81*, 74–81. [CrossRef]
31. Sonnerup, B.Ö.; Cahill, L., Jr. Magnetopause structure and attitude from Explorer 12 observations. *J. Geophys. Res.* **1967**, *72*, 171–183. [CrossRef]
32. De Hoffmann, F.; Teller, E. Magneto-hydrodynamic shocks. *Phys. Rev.* **1950**, *80*, 692. [CrossRef]
33. Regi, M.; Del Corpo, A.; De Lauretis, M. The use of the empirical mode decomposition for the identification of mean field aligned reference frames. *Ann. Geophys.* **2016**, *59*. [CrossRef]
34. Bruno, R.; Bavassano, B.; Villante, U. Evidence for long period Alfvén waves in the inner solar system. *J. Geophys. Res. Space Phys.* **1985**, *90*, 4373–4377. [CrossRef]
35. Tsurutani, B.T.; Echer, E.; Gonzalez, W.D. The solar and interplanetary causes of the recent minimum in geomagnetic activity (MGA23): A combination of midlatitude small coronal holes, low IMF B_Z variances, low solar wind speeds and low solar magnetic fields. *Ann. Geophys.* **2011**, *29*, 839–849. [CrossRef]

36. Elsasser, W.M. Hydromagnetic Dynamo Theory. *Rev. Mod. Phys.* **1956**, *28*, 135–163. [CrossRef]
37. Bruno, R.; Carbone, V. The solar wind as a turbulence laboratory. *Living Rev. Sol. Phys.* **2013**, *10*, 1–208. [CrossRef]
38. Huang, N.E.; Shen, Z.; Long, S.R.; Wu, M.C.; Shih, H.H.; Zheng, Q.; Yen, N.C.; Tung, C.C.; Liu, H.H. The empirical mode decomposition and the Hilbert spectrum for nonlinear and non-stationary time series analysis. *Proc. R. Soc. Lond. Ser. A Math. Phys. Eng. Sci.* **1998**, *454*, 903–995. [CrossRef]
39. Flandrin, P.; Rilling, G.; Goncalves, P. Empirical mode decomposition as a filter bank. *IEEE Signal Process. Lett.* **2004**, *11*, 112–114. [CrossRef]
40. Rilling, G.; Flandrin, P.; Goncalves, P. On empirical mode decomposition and its algorithms. In Proceedings of the IEEE-EURASIP Workshop on Nonlinear Signal and Image Processing, Grado-Trieste, Italy, 8–11 June 2003; Volume 3, pp. 8–11.
41. Grappin, R.; Mangeney, A.; Marsch, E. On the origin of solar wind MHD turbulence: Helios data revisited. *J. Geophys. Res. Space Phys.* **1990**, *95*, 8197–8209. [CrossRef]
42. Grinsted, A.; Moore, J.C.; Jevrejeva, S. Application of the cross wavelet transform and wavelet coherence to geophysical time series. *Nonlinear Process. Geophys.* **2004**, *11*, 561–566. [CrossRef]
43. Magyar, N.; Van Doorsselaere, T.; Goossens, M. The nature of Elsässer variables in compressible MHD. *Astrophys. J.* **2019**, *873*, 56. [CrossRef]
44. Snekvik, K.; Tanskanen, E.I.; Kilpua, E.K.J. An automated identification method for Alfvénic streams and their geoeffectiveness. *J. Geophys. Res. Space Phys.* **2013**, *118*, 5986–5998. [CrossRef]
45. Prölss, G.W. Ionospheric F-region storms. In *Handbook of Atmospheric Electrodynamics*, 1st ed.; Volland, H., Ed. ; CRC Press: Boca Raton, FL, USA, 1995; Chapter 8, pp. 195–248. [CrossRef]
46. Spogli, L.; Sabbagh, D.; Regi, M.; Cesaroni, C.; Perrone, L.; Alfonsi, L.; Di Mauro, D.; Lepidi, S.; Campuzano, S.A.; Marchetti, D.; et al. Ionospheric Response Over Brazil to the August 2018 Geomagnetic Storm as Probed by CSES-01 and Swarm Satellites and by Local Ground-Based Observations. *J. Geophys. Res. Space Phys.* **2021**, *126*, e2020JA028368. [CrossRef]
47. Alfonsi, L.; Cesaroni, C.; Spogli, L.; Regi, M.; Paul, A.; Ray, S.; Lepidi, S.; Di Mauro, D.; Haralambous, H.; Oikonomou, C.; et al. Ionospheric Disturbances Over the Indian Sector During 8 September 2017 Geomagnetic Storm: Plasma Structuring and Propagation. *Space Weather* **2021**, *19*, e2020SW002607. [CrossRef]
48. Regi, M.; Redaelli, G.; Francia, P.; De Lauretis, M. ULF geomagnetic activity effects on tropospheric temperature, specific humidity, and cloud cover in Antarctica, during 2003–2010. *J. Geophys. Res. Atmos.* **2017**, *122*, 6488–6501. [CrossRef]
49. Voiculescu, M.; Usoskin, I.; Condurache-Bota, S. Clouds blown by the solar wind. *Environ. Res. Lett.* **2013**, *8*, 045032. [CrossRef]